RESEARCH ARTICLE

A Decentralized Control With Adaptive Virtual Inertia and Damping Combination for Islanded Cascaded-Type VSG Systems

LANG LI[ID], KE ZHOU, AND PENG TIAN
Department of Automation, Moutai Institute, Renhuai 564507, China

Corresponding author: Ke Zhou (zhouke@mtxy.edu.cn)

ABSTRACT With the increase of distributed generations, the problems related to lack of inertia and damping support for cascaded-type power networks are becoming more and more prominent. This may lead to oscillation and even system instability. To address this problem, a decentralized control with adaptive virtual inertia and damping combination method is proposed for islanded cascaded-type virtual synchronous generator (VSG) systems. Firstly, a model of islanded cascaded-type VSGs was developed to analyze the impact of changes in inertia and damping coefficients on frequency characteristics during dynamic processes. Subsequently, a decentralized control was proposed, which employs an adaptive method for regulating inertia and damping coefficients in real-time. The scheme effectively suppresses power and frequency oscillation, leading to improved dynamic frequency performance. Furthermore, this decentralized strategy only requires the local voltage and current measurements, ensuring a fully decentralized implementation. The cascaded-type VSGs demonstrate satisfactory reliability. The stability of the proposed strategy has been demonstrated, and guidelines for designing key control coefficients have been validated through the Lyapunov energy function method. Simulation and experimental results validate the proposed method.

INDEX TERMS Cascaded-type VSGs, decentralized control, virtual inertia and damping combination.

I. INTRODUCTION

With the growing concerns regarding the energy crisis and environmental pollution [1], [2], much attention has been directed towards the electric power system that comprises distributed generations (DGs) [3], [4]. In contrast to the traditional synchronous generators (SGs), the inverter-based DGs with conventional control methods obviously differ in external characteristics. Notably, these DGs demonstrate remarkable response speed and virtually no moment of inertia [5], [6].

With the increasing penetration of large-scale DGs, their low inertia and poor damping characteristics have become

The associate editor coordinating the review of this manuscript and approving it for publication was Chi-Seng Lam[ID].

prominent issues [7]. In the event of a disturbance, the system may experience oscillations and even collapse [8]. To address this problem, the VSG technology has gained significant attention [9], [10]. The core idea is to imitate the swing equation to provide the necessary inertia and damping support [11], [12]. This technology enables power-sharing, frequency regulating, and power oscillation suppression [13].

People have gradually become more interested in the research on the frequency oscillation suppression control and power oscillation suppression control of VSGs [14]. Currently, research on oscillation suppression control of VSG is mainly divided into two aspects. The first aspect is paralleled-type VSGs, which involve connecting multiple VSGs in parallel [15]. It can operate in grid-connected mode or islanded mode [5], [6]. Damping-based methods [16], [17]

were presented to dampen oscillations of the system. In [16], a reference-feedforward-based damping control method is proposed. This method could adaptively tune the real-time damping parameters without influencing the initial inertial response. In [17], an active power oscillation damping control is proposed for paralleled-type VSGs through an acceleration control method. Then, inertia-based strategies were introduced [18], [19]. The adaptation control scheme of virtual inertia was presented in [18] to suppress the frequency oscillation. Design guidelines based on stability analysis were given in detail. In [19], a data-based intelligent virtual inertia method is proposed that can decrease both frequency drop and the rate of change of frequency (RoCoF). In [20], the bang-bang inertia method, which has good frequency response characteristics and robustness, is introduced. Next, the fuzzy adaptive inertia control [21] and the neural network optimization inertia control [22] were proposed to optimize the inertia parameter. The inertia and damping combined control strategy was proposed to take full advantage of the freedom of adjustment [23]. Additionally, in [24], the output impedance was shaped through a virtual impedance controller to improve the mismatched transmission line impedance, and then power oscillation was damped. The damping-based, inertia-based, inertia-and-damping combination control and virtual impedance-based methods could effectively improve the dynamic oscillation. However, these methods are only available for paralleled-type VSGs.

The second aspect is the use of cascaded-type VSGs. A medium or high-voltage system can be formed in the series by connecting low-voltage modules [25], [26], such as photovoltaics (PVs) and energy storage devices. A self-synchronized control scheme was proposed [27] for the cascaded-type power network without requiring communications, allowing for stable operation under resistance-inductance (RL) loads. Furthermore, [28] proposed a control strategy to expand the application scope of RL loads and resistance-capacitance (RC) loads. However, this strategy might lead to multiple equilibrium operation points. In response, [29] proposed a self-synchronized way with a unique equilibrium point. Despite the previous proposals for decentralized self-synchronized control schemes for cascaded-type power networks, they could not provide inertia and damping. Thus, the cascaded-type power network was prone to oscillation or instability when disturbances occurred. In order to expand the concept of VSG to a cascaded-type power network, [30] proposed a communication-free mutual damping control method to dampen oscillation. Additionally, [31] presented a communication-free J-adaptive and D-fixed control scheme. However, these proposals did not use the regulation degree of inertia and damping coefficient in real-time, and there is room for further improvement in the performance of power and frequency oscillation.

To address the aforementioned problem, this paper proposes a decentralized control featuring an adaptive combination of virtual inertia and damping. The proposed controller can be established only with the local voltage and current information, making it a communication-free method. The islanded cascaded-type VSG systems hold improved reliability. Meanwhile, the utilization of real-time inertia and damping coefficients contributes to enhancing dynamic frequency response and mitigating frequency oscillations. The main contributions of this paper are as follows:

1) The impacts of variations in virtual inertia and damping on the dynamic frequency characteristics of cascaded-type VSGs are revealed. The maximum initial RoCoF in a specific VSG is primarily determined by its virtual inertia term, while the damping term hardly affects its RoCoF. Changes in the virtual damping parameter influence the steady-state error of frequency and the system's adjusting time.

2) A decentralized control approach is proposed, which combines adaptive virtual inertia and damping, to enhance the dynamic performance of systems. The proposed method effectively dampens power and frequency oscillations of islanded cascaded-type VSGs.

For convenience, the abbreviations are summarized in Table 1.

TABLE 1. List of abbreviations.

Abbreviation	Meaning
DGs	Distributed generations
SGs	Synchronous generators
VSG	Virtual synchronous generator
RoCoF	Rate of change of frequency
PVs	Photovoltaics
RL	Resistance-inductance
RC	Resistance-capacitance
PLL	Phase-locked loop
RCP	Rapid Control Prototyping

The rest of this article is arranged as follows. Section II presents the model and dynamic frequency characteristic analysis of cascaded-type VSGs. Section III describes the proposed decentralized adaptive control scheme, whose stability is proved in Section IV. Section V and Section VI explain simulation results and experimental results. Finally, Section VII summarizes this article.

II. MODEL AND DYNAMIC FREQUENCY CHARACTERISTIC ANALYSIS OF CASCADED-TYPE VSGs
A. CASCADED-TYPE VSGS
The cascaded-type VSGs shown in Fig. 1 consist of n DGs that are connected in series/cascade. Each DG includes a low-pass filter that enables independent voltage source control for the inverters.

The self-synchronized $P - \omega$ control for cascaded-type microgrids is [28]:

$$\omega_i = \omega^* + \frac{m_i}{\tau_i s + 1} \text{sgn}(Q_i)(P_i - P^*) \tag{1}$$

$$V_i = V^* \tag{2}$$

where ω_i and ω^* represent the actual and nominal angular frequency, V_i and V^* signify the actual and nominal
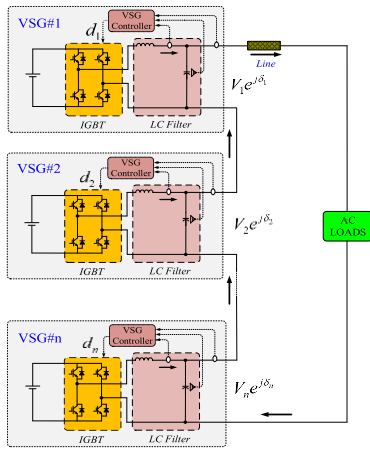
FIGURE 1. Schematic of cascaded-type VSGs.

voltage amplitudes, P^* means the nominal active power, τ_i is the filter's time constant, sgn $(\cdot)$ represents a sign function. m_i represents a positive constant. The self-synchronized mechanism of the islanded cascaded-type microgrids highly depends on load characteristics. Under the RL loads, the inverse droop is applied, while the droop control is used under the RC loads.

Rewrite (1) as follows:

$$\frac{\tau_i}{m_i}\frac{d\omega_{Di}}{dt} = \text{sgn}\,(Q_i)\,(P_i - P^*) - \frac{1}{m_i}\omega_{Di} \quad (3)$$

where ω_{Di} denotes the angular frequency difference, and $\omega_{Di} = \omega_i - \omega^*$. By comparing the 2-order swing equation of SGs [18] and (3), the virtual inertia J_i and damping D_i coefficients can be written as (4).

$$J_i = \frac{\tau_i}{m_i},\ D_i = \frac{1}{m_i} \quad (4)$$

From (3) and (4), the cascaded-type VSG model of the ith module is represented as:

$$J_i\frac{d\omega_{Di}}{dt} = \text{sgn}\,(Q_i)\,(P_i - P^*) - D_i\omega_{Di} \quad (5)$$

From a physical meaning standpoint, the model of (5) is convenient for inertia and damping parameters designing. The cascaded-type VSGs incorporate multiple VSGs in a series connection, which differs from cascade multi-level converter VSGs. The cascade multi-level converters have a general LC filter, which can be viewed as a single VSG.

B. ANALYSIS OF THE DYNAMIC FREQUENCY CHARACTERISTICS

From [28], the expression of active power P_i and reactive power is,

$$P_i = \frac{V_i}{Z_{load}}\sum_{j=1}^{n} V_j \cos\,(\delta_i - \delta_j + \theta_{load}) \quad (6)$$

$$Q_i = \frac{V_i}{Z_{load}}\sum_{j=1}^{n} V_j \sin\,(\delta_i - \delta_j + \theta_{load}) \quad (7)$$

where δ_i is a voltage phase-angle. Z_{load} and θ_{load} mean load impedance module and phase angle. By substituting (2) into (6), we have,

$$P_i = \kappa \cos\theta_{load}\sum_{j=1}^{n} \cos\,(\delta_i - \delta_j) - \kappa \sin\theta_{load}\sum_{j=1}^{n} \sin\,(\delta_i - \delta_j) \quad (8)$$

where $\kappa = (V^*)^2\big/Z_{load}$. Ignoring the transmission line, the load demands P_{load} and Q_{load} are written as,

$$P_{load} = n^2\kappa \cos\theta_{load},\ Q_{load} = n^2\kappa \sin\theta_{load} \quad (9)$$

Combining (8) and (9), we have

$$P_i = \frac{1}{n^2}P_{load}\sum_{j=1}^{n} \cos\,(\delta_i - \delta_j) - \frac{1}{n^2}Q_{load}\sum_{j=1}^{n} \sin\,(\delta_i - \delta_j) \quad (10)$$

From (10), the small-signal model expresses as,

$$\Delta P_i = \alpha_i\Delta P_{load} - \sum_{j=1}^{n} \beta_{ij}\,(\Delta\delta_i - \Delta\delta_j) \quad (11)$$

where

$$\begin{cases} \alpha_i = \dfrac{1}{n^2}\displaystyle\sum_{j=1}^{n} \cos\,(\delta_{ij}^o) \\[2mm] \beta_{ij} = \dfrac{1}{n^2}P_{load}^o \sin\,(\delta_{ij}^o) + \dfrac{1}{n^2}Q_{load} \cos\,(\delta_{ij}^o) \end{cases} \quad (12)$$

where superscript "o" means its related initial value, $\delta_{ij}^o = \delta_i^o - \delta_j^o$. Q_{load} is a constant.

From $\Delta\omega_{Di} = \Delta\omega_i$, $\omega_i = \dot{\delta}_i$, we have,

$$\Delta\delta_i = \frac{1}{s}\Delta\omega_{Di} \quad (13)$$

(13) From (13) and (11), yields,

$$s\Delta P_i = s\alpha_i\Delta P_{load} - \sum_{j=1}^{n} \beta_{ij}\,(\Delta\omega_{Di} - \Delta\omega_{Dj}) \quad (14)$$

Equation (5) is rewritten as,

$$\Delta\omega_{Di} = \frac{\text{sgn}\,(Q_i)\,\Delta P_i}{(J_i s + D_i)} \quad (15)$$

Take two VSGs as an example, and the system's load is an RL load. From (14) and (15), we have,

$$\begin{cases} s\Delta P_1 = s\alpha_1\Delta P_{load} - \beta_{12}\,(\Delta\omega_{D1} - \Delta\omega_{D2}) \\ s\Delta P_2 = s\alpha_2\Delta P_{load} - \beta_{21}\,(\Delta\omega_{D2} - \Delta\omega_{D1}) \\ (J_1 s + D_1)\,\Delta\omega_{D1} = \Delta P_1 \\ (J_2 s + D_2)\,\Delta\omega_{D2} = \Delta P_2 \end{cases} \quad (16)$$

Then, we can get the transfer function $G\,(s) = \Delta\omega_D\big/\Delta P_{load}$,

$$G\,(s) = \frac{\Delta\omega_{D1}}{\Delta P_{load}} = \frac{J_2\alpha_1 s^3 + D_2\alpha_1 s^2 + (\beta_{21}\alpha_1 + \alpha_2\beta_{12})\,s}{J_1 J_2 s^4 + as^3 + bs^2 + cs} \quad (17)$$

where

$$a = J_1 D_2 + J_2 D_1 \tag{18}$$

$$b = J_1 \beta_{21} + D_1 D_2 + J_2 \beta_{12} \tag{19}$$

$$c = D_1 \beta_{21} + D_2 \beta_{12} \tag{20}$$

According to (17), the Bode Diagram method is applied to analyze the impact of variations in inertia and damping on dynamic frequency. The Bode Diagram of magnitude-frequency characteristic in the low-frequency interval shows the steady-state frequency deviation. The high-frequency curve presents the initial values of the RoCoF. Let $D_1 = 100, D_2 = 50, J_2 = 25$, the Bode Diagram for three different values of J_1 is presented in Fig. 2(a). When $D_1 = 100, D_2 = 50, J_1 = 20$, Bode Diagram is presented in Fig. 2(b) for three different values of J_2. From Fig. 2, a larger J_1 contributes to decreasing the initial RoCoF of VSG#1, however, variations of J_2 have a minor influence on the initial RoCoF of VSG#1. When the parameters (J and D) of both VSGs are the same, values of the initial RoCoF for the two DGs are the same. Therefore, the conclusion can be drawn as follows: 1) the virtual inertia parameter primarily affects its own maximum initial RoCoF; 2) Different J_1 and J_2 have a minor influence on the steady-state frequency deviation; 3) the different resonance peak values can reflect the oscillation frequency and magnitude.
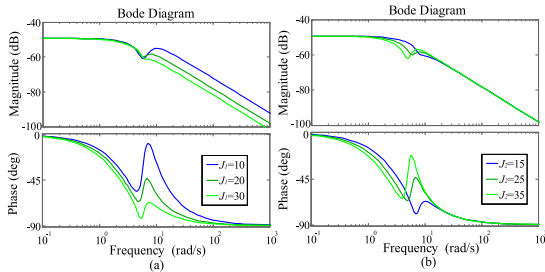
FIGURE 2. Bode diagram of $G(s)$ with (a) J_1 variations, (b) J_2 variations.

The corresponding comparison results of three different J_1 and J_2 are presented in Fig. 3, which verifies this conclusion. Under the constant load power, the caparison results of the three different conditions ($J_1 = 10, J_2 = 25; J_1 = 20, J_2 = 25; J_1 = 30, J_2 = 25$) are present in Fig. 3(a). Similarly, the other comparison results are shown in Fig. 3(b) ($J_1 = 20, J_2 = 15; J_1 = 20, J_2 = 25; J_1 = 20, J_2 = 35$). The RoCoF is calculated by (26), which will be explained in Section III Part B. For example, in Fig. 3(a), compared to $J_1 = 10, J_2 = 25$, the initial RoCoF is greater than $J_1 = 20, J_2 = 25$, and they hold different oscillation frequencies and magnitudes. In addition, the steady-state frequency of the three conditions is equal. The bode diagram of (17) is presented in Fig. 4(a) as D_1 changes, and $J_1 = 20, D_2 = 50, J_2 = 25$. When $D_1 = 100, J_1 = 20, J_2 = 25$, the bode diagram with D_1 variations is shown in Fig. 4(b). Different damping coefficients have little influence on initial RoCoF. However, they do affect the equilibrium point of frequency.

Increasing the damping coefficient can reduce the resonance peak value and the adjusting time. The comparison results in Fig. 5 confirm the above conclusions.
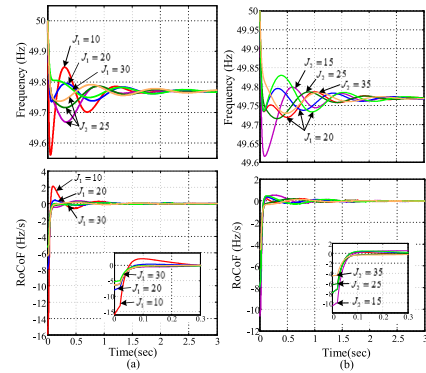
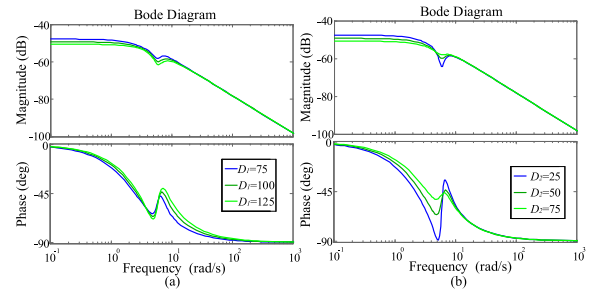**FIGURE 3.** Comparison results of frequency and RoCoF with (a) J_1 variations, (b) J_2 variations.

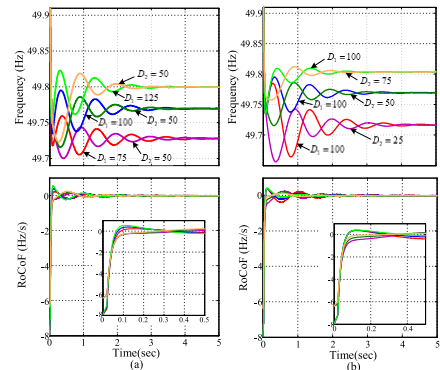**FIGURE 4.** Bode diagram of G(s) with (a) D_1 variations, (b) D_2 variations.

FIGURE 5. Comparison results of frequency and RoCoF with (a) D_1 variations, (b) D_2 variations.

As described above, the frequency characteristics in the dynamic process can be summarized as follows: 1) adjusting the virtual inertia parameter of the ith VSG mainly affects its maximum initial RoCoF. Changes in the damping parameter hardly affect the maximum initial RoCoF; 2) adjusting virtual damping influences the frequency equilibrium value and the adjusting time.

From (17), the root locus diagrams with changes in the control parameter of J_1, J_2, D_1, D_2 are displayed in Fig. 6(a), (b), (c) and (d), respectively. As seen, the system is stable.

III. PROPOSED CONTROL METHOD

A. PROPOSED DECENTRALIZED CONTROL WITH ADAPTIVE VIRTUAL INERTIA AND DAMPING COMBINATION

The proposed decentralized control with adaptive virtual inertia and damping combination is introduced in this section. From (5), the proposed adaptive virtual inertia and damping combination control scheme is constructed as follows,

$$J_i = J_{0i} + k_J \left(\omega_i - \omega_{com,i} \right) \frac{d\omega_{Di}}{dt} \qquad (21)$$

$$D_i = D_{0i} e^{k_D \left(\omega_i - \omega_{com,i} \right)} \qquad (22)$$

where J_{0i} and D_{0i} signify the nominal inertia and damping term. k_J and k_D mean the positive coefficient. $\omega_{com,i}$ means the angular frequency of the current of the transmission line through a phase-locked loop (PLL) of VSG#i. From subscripts in (21) and (22), the proposed method is a fully decentralized way. From (21) and (22), the inertia and damping coefficients change adaptively in real-time based on $\left(\omega_i - \omega_{com,i} \right)$.

Due to the series structure, there is,

$$\omega_{com,i} = \omega_{com,j} = \omega_{com} \qquad (23)$$

From (23), $\omega_{com,i}$ is the global variable. All VSGs can construct their virtual inertia and damping term based on this global variable. In the steady state, from (21) and (22), $\omega_i = \omega_j = \omega_{com}$, $J_i = J_{0i}, D_i = D_{0i}$. According to (1), $\delta_i^o = \delta_j^o$, the different VSGs hold equal phase angles. Combining (2), the load voltages are equivalent to the aggregate of all VSG voltages. Therefore, the proposed scheme optimizes the dynamic frequency performance but does not affect the steady state.

The dynamic variation diagram of ω_i is presented in Fig. 7. The oscillations are divided into four intervals:$[t_0, t_1]$, $[t_1, t_2]$, $[t_2, t_3]$, $[t_3, t_4]$. The required control laws of J_i and D_i in the different inverters are listed in Table 2.

TABLE 2. Control laws in the different intervals.

Interval	$\omega_i - \omega_{com,i}$	$d\omega_{Di}/dt$	J_i	D_i
$[t_0, t_1]$	$\omega_i - \omega_{com,i} > 0$	$d\omega_{Di}/dt > 0$	Increasing	Increasing
$[t_1, t_2]$	$\omega_i - \omega_{com,i} > 0$	$d\omega_{Di}/dt < 0$	Decreasing	Increasing
$[t_2, t_3]$	$\omega_i - \omega_{com,i} < 0$	$d\omega_{Di}/dt < 0$	Increasing	Decreasing
$[t_3, t_4]$	$\omega_i - \omega_{com,i} < 0$	$d\omega_{Di}/dt > 0$	Decreasing	Decreasing

The control lows of J_i. In $[t_0, t_1]$ and $[t_2, t_3]$, the angular frequency ω_i deviates from $\omega_{com,i}$, a larger J_i will conduce to decrease frequency deviations. Similarly, in $[t_1, t_2]$ and $[t_3, t_4]$, the ω_i tends to return $\omega_{com,i}$, a smaller J_i will help accelerate ω_i returning to $\omega_{com,i}$. The control lows of D_i. In the first and the second intervals, the angular frequency
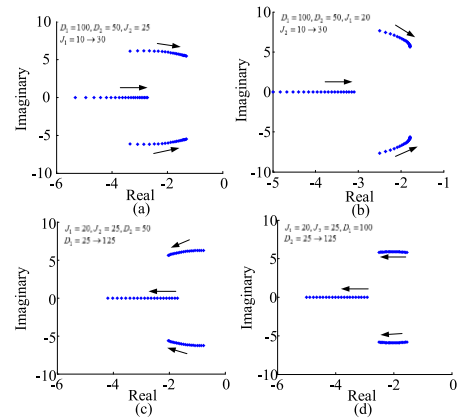

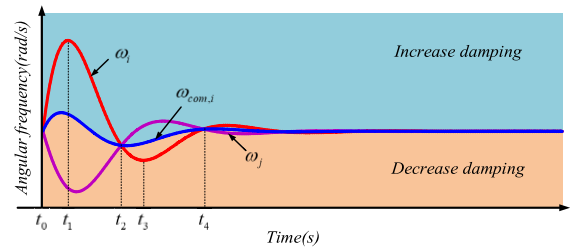**FIGURE 6.** Root locus with changes of (a) J_1, (b) J_2, (c) D_1, (d) D_2.

FIGURE 7. Dynamic variation diagram of ω_i.

ω_i is greater than $\omega_{com,i}$, and a larger damping coefficient is required to slow down ω_i. On the contrary, in the third and fourth intervals, ω_i is less than $\omega_{com,i}$, a smaller damping term is needed to make ω_i accelerate. In summary, the control method of the proposed scheme is to make ω_i align with $\omega_{com,i}$. Thus, the power and frequency oscillation is damped.

B. ACQUIRING OF THE DIFFERENTIAL TERM

Direct calculation of the differential term $d\omega_{Di}/dt$ may bring out measurement noises. To solve that, the acquiring of $d\omega_{Di}/dt$ is introduced in the next. Substitute (21) into (5), then,

$$\left[J_{0i} + k_J \left(\omega_i - \omega_{com,i} \right) \frac{d\omega_{Di}}{dt} \right] \frac{d\omega_{Di}}{dt} = \mathrm{sgn}\left(Q_i \right) P_{Di} - D_i \omega_{Di} \qquad (24)$$

where $P_{Di} = P_i - P^*$. From the control lows in Table 1, solving (24), yields,

$$\frac{d\omega_{Di}}{dt} = \frac{-J_{0i} + \sqrt{J_{0i}^2 + 4k_J \left(\omega_i - \omega_{com,i} \right) \left(\mathrm{sgn}\left(Q_i \right) P_{Di} - D_i \omega_{Di} \right)}}{2k_J \left(\omega_i - \omega_{com,i} \right)} \qquad (25)$$

To avoid singularity, substituting (22) into (25), yields, (26), as shown at the bottom of the next page.
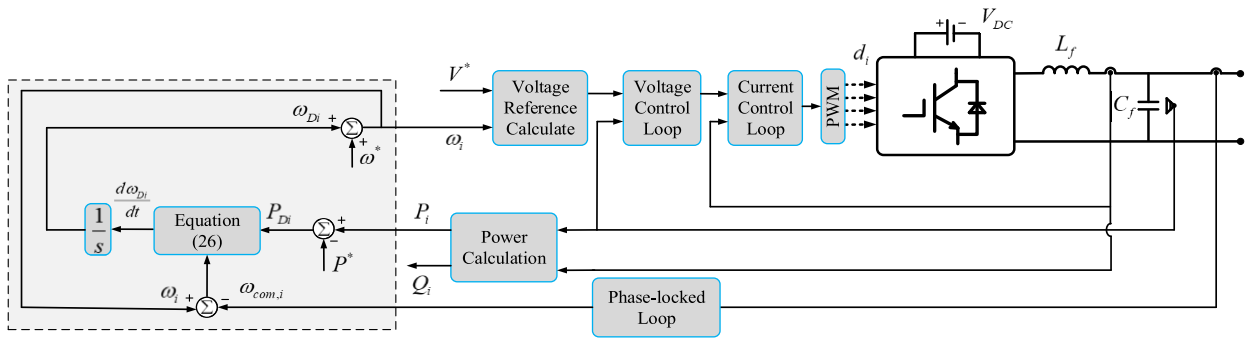
FIGURE 8. Control block diagram of the proposed method.

Therefore, the term $d\omega_{Di}/dt$ is obtained by (26) without derivative action. The control block diagram of the proposed method is depicted in Fig. 8, in which L_f, C_f represent the filter inductor and capacitor. d_i and V_{DC} are the duty cycle and the voltage at the DC side.

IV. STABILITY ANALYSIS

To verify the stability of the proposed scheme and give the design ranges of key control parameters, the stability analysis of the proposed control strategy is carried out in this section using the Lyapunov energy function method [32].

Transmission line current rewrites as:

$$Ie^{j\delta_{com}} = \frac{\sum_{j=1}^{n} V_j e^{j\delta_j}}{Z_{load} e^{j\theta_{load}}} = \frac{V^*}{Z_{load}} \sum_{j=1}^{n} e^{j(\delta_j - \theta_{load})} \quad (27)$$

where I and δ_{com} are the current amplitudes and phase angles. Equation (27) can be expressed as,

$$\cos \delta_{com} = \sum_{j=1}^{n} \cos(\delta_j - \theta_{load}) \quad (28)$$

$$\sin \delta_{com} = \sum_{j=1}^{n} \sin(\delta_j - \theta_{load}) \quad (29)$$

Then, the phase-angle δ_{com} writes:

$$\dot{\delta}_{com} = \frac{1}{n} \sum_{j=1}^{n} \dot{\delta}_j \quad (30)$$

Equation (30) is rewritten as:

$$\omega_{com} = \frac{1}{n} \sum_{j=1}^{n} \omega_j \quad (31)$$

Substituting (2) into (6), we can get,

$$P_i = \frac{(V^*)^2}{Z_{load}}$$
$$\sum_{j=1}^{n} \left[\cos(\delta_i - \delta_j) \cos \theta_{load} - \sin(\delta_i - \delta_j) \sin \theta_{load} \right]$$
$$\quad (32)$$

Usually, $\delta_i - \delta_j \leq \theta_{load}$, (32) becomes (33).

$$P_i = a - b \sum_{j=1}^{n} \sin(\delta_i - \delta_j) \quad (33)$$

where

$$a = \frac{n(V^*)^2 \cos \theta_{load}}{Z_{load}} \quad (34)$$

$$b = \frac{(V^*)^2 \sin \theta_{load}}{Z_{load}} \quad (35)$$

Substituting (33), (34) and (35) into (24), we have,

$$J_{0i}\dot{\omega}_{Di} = \text{sgn}(Q_i) \left(a - P^* - b \sum_{j=1}^{n} \sin(\delta_i - \delta_j) \right)$$
$$- D_{0i} e^{\frac{k_D}{n} \sum_{j=1}^{n} (\omega_j - \omega_j)} \omega_{Di} - \frac{k_J}{n} (\dot{\omega}_{Di})^2 \sum_{j=1}^{n} (\omega_j - \omega_j)$$
$$\quad (36)$$

The constructed Lyapunov energy function E_{Ly} is,

$$E_{Ly} = E_p + E_k \quad (37)$$

where E_P is the potential-energy function, E_k is the kinetic-energy function. They can rewrite,

$$E_k = \frac{1}{2} \sum J_{0i} \omega_{Di}^2 \quad (38)$$

$$\frac{d\omega_{Di}}{dt} = \frac{2 \left(\text{sgn}(Q_i) P_{Di} - D_{0i} e^{k_D(\omega_i - \omega_{com,i})} \omega_{Di} \right)}{J_{0i} + \sqrt{J_{0i}^2 + 4k_J (\omega_i - \omega_{com,i}) \left(\text{sgn}(Q_i) P_{Di} - D_{0i} e^{k_D(\omega_i - \omega_{com,i})} \omega_{Di} \right)}} \quad (26)$$

$$E_P = \text{sgn}(Q_i) \times$$

$$\left\{ -\sum_{i=1}^{n} (a - P^*) \left(\delta_i - \delta_i^o \right) \right.$$

$$\left. -b \sum_{i=1}^{n-1} \sum_{j=i+1}^{n} \left[\cos(\delta_i - \delta_j) - \cos\left(\delta_i^o - \delta_j^o \right) \right] \right\} \quad (39)$$

Combining (36), (38) and (39), we can get,

$$\dot{E}_{Ly} = -\sum_{i=1}^{n} \left(D_{0i} e^{\frac{k_D}{n} \sum_{j=1}^{n} (\omega_i - \omega_j)} \omega_{Di}^2 \right)$$

$$- \frac{k_J}{n} \sum_{i=1}^{n} \omega_{Di} (\dot{\omega}_{Di})^2 \sum_{j=1}^{n} (\omega_{Di} - \omega_{Dj}) \quad (40)$$

Rewrite (40) as the matrix, yields,

$$\dot{E}_{Ly} = -\boldsymbol{\omega}^{\mathbf{T}} \left[\mathbf{D} + \frac{1}{2} (\boldsymbol{\Psi}\mathbf{L} + \mathbf{L}\boldsymbol{\Psi}) \right] \boldsymbol{\omega} \quad (41)$$

where

$$\boldsymbol{\omega}^{\mathbf{T}} = [\omega_{D1}, \omega_{D2}, \cdots \omega_{Dn}]^T \quad (42)$$

$$\boldsymbol{\Psi} = \frac{k_J}{n} diag \left[(\dot{\omega}_{D1})^2, (\dot{\omega}_{D2})^2, \cdots (\dot{\omega}_{Dn})^2 \right]^T \quad (43)$$

$$\mathbf{D} = diag \left[D_{01} e^{\gamma_1}, D_{02} e^{\gamma_2}, \cdots D_{0n} e^{\gamma_n} \right]^T \quad (44)$$

$$\gamma_i = \frac{k_D}{n} \sum_{j=1}^{n} (\omega_i - \omega_j) \quad (45)$$

$$\mathbf{L} = n\mathbf{E}_{n \times n} - \mathbf{I}_{n \times n} \quad (46)$$

where $\mathbf{E}_{n \times n} = diag[1, 1, \cdots 1]$. $\mathbf{I}_\mathbf{n}$ is the all-one matrix, in which all elements are 1.

Let that λ_i is the eigenvalues of the matrix. For a $n \times n$ matrix $\mathbf{A}$, the spectral radius $\rho(\mathbf{A})$ is expressed as $\rho(\mathbf{A}) = \max |\lambda_i|$ $(i = 1, \cdots n)$. In addition, $\rho(\mathbf{A}) \leq \|\mathbf{A}\|$, where $\|\mathbf{A}\|$ is the norm of $\mathbf{A}$. Then, there is,

$$\rho \left(\frac{1}{2} (\boldsymbol{\Psi}\mathbf{L} + \mathbf{L}\boldsymbol{\Psi}) \right)$$

$$\leq \left\| \frac{1}{2} (\boldsymbol{\Psi}\mathbf{L} + \mathbf{L}\boldsymbol{\Psi}) \right\| \leq \|\boldsymbol{\Psi}\| \|\mathbf{L}\| \leq \zeta_{\max} \|\mathbf{L}\| \quad (47)$$

where $\zeta_{\max}$ is the maximum element of the matrix $\boldsymbol{\Psi}$. Define that $d_{\min}$ is the minimum damping for all VSGs, *i.e.*, $d_{\min} \leq \min_{i=1,\cdots,n} \{D_{0i} e^{\gamma_i}\}$. If $\zeta_{\max} \|\mathbf{L}\| < d_{\min}$, (47) is rewritten as,

$$\rho \left(\frac{1}{2} (\boldsymbol{\Psi}\mathbf{L} + \mathbf{L}\boldsymbol{\Psi}) \right) < d_{\min} \quad (48)$$

In addition, for the symmetric matrix $(\boldsymbol{\Psi}\mathbf{L} + \mathbf{L}\boldsymbol{\Psi})$ and $\mathbf{D}$, we have,

$$\lambda \left(\mathbf{D} + \frac{1}{2} (\boldsymbol{\Psi}\mathbf{L} + \mathbf{L}\boldsymbol{\Psi}) \right) > 0 \quad (49)$$

The matrix $\mathbf{D} + \frac{1}{2} (\boldsymbol{\Psi}\mathbf{L} + \mathbf{L}\boldsymbol{\Psi})$ is a symmetric positive matrix. Thus, there is,

$$\dot{E}_{Ly} = -\boldsymbol{\omega}^{\mathbf{T}} \left[\mathbf{D} + \frac{1}{2} (\boldsymbol{\Psi}\mathbf{L} + \mathbf{L}\boldsymbol{\Psi}) \right] \boldsymbol{\omega} < 0 \quad (50)$$

From (50), E_{Ly} is damped. Therefore, the proposed strategy is stable. Stability proof completed.

The design control parameters should satisfy,

$$\zeta_{\max} \|\mathbf{L}\| < d_{\min} \quad (51)$$

$$d_{\min} \leq \min_{i=1,\cdots,n} \left\{ D_{0i} e^{k_D (\omega_i - \omega_{com,i})} \right\} \quad (52)$$

Define that $RoCoF_{\max}$ is the permissible maximum RoCoF values for VSGs. Combining $\|\mathbf{L}\| = n$, (43) and (51), we have,

$$0 < k_J < \frac{d_{\min}}{RoCoF_{\max}^2} \quad (53)$$

From (52), we can get,

$$0 < k_D \leq \frac{\left| \ln \frac{d_{\min}}{D_{0i}} \right|}{\left| \min_{i=1,\cdots,n} (\omega_i - \omega_{com,i}) \right|} \quad (54)$$

Therefore, the control parameters should satisfy (53) and (54) to maintain the stable operating. The design ranges of the adaptive control coefficients for the proposed control method are provided.

V. SIMULATIONS

A 3-cascaded VSG is implemented in this section to demonstrate the feasibility of the proposed method. Based on the Matlab/Simulink SimPowerSystems platform, simulations are implemented, and Table 3 presents the related parameters.

TABLE 3. Parameters for simulations.

Variable	Values	Variable	Values
V^* (V)	$311\sqrt{2}/3$	C_f (μF)	20
P^* (W)	1000	L_f (H)	1.5e-3
ω^* (rad/s)	100π	V_{dc} (V)	200

TABLE 4. Quantitative comparisons.

Control method	Adjusting time	Maximum RoCoF
J-fixed and D-fixed	3.2s in [0s,5s] 2.5s in [5s, 10s]	5.3Hz/s
J-adaptive and D-fixed	2.8s in [0s,5s] 2s in [5s, 10s]	2.7Hz/s
J-adaptive and D-adaptive	2s in [0s,5s] 1.6s in [5s, 10s]	2.3Hz/s

A. CASE 1:SIMULATION WITH J-FIXED AND D-FIXED CONDITION

This case is performed with the J-fixed ($k_J = 0$) and D-fixed ($k_D = 0$) situation, where $D_1 = D_2 = D_3 = 100$, $J_1 = 15, J_2 = 30, J_3 = 45$. Simulation results of P_i, f_i, RoCoF and J/D parameters are exhibited in Fig. 9(a), (b), (c) and (d). For [0s, 5s], the system's adjusting time is about 3.2s, which is about 2.5s in the interval [5s, 10s]. After t=5s, the maximum RoCoF is about 5.3Hz/s. Figure 9(e) shows the voltage and current waveforms, and reactive powers are presented in Fig. 9(f). Therefore, the power and frequency oscillations occur with the fixed virtual inertia (J-fixed) and fixed damping (D-fixed) control.

B. CASE 2:SIMULATION WITH J-ADAPTIVE AND D-FIXED CONDITION

This case is carried out with the adaptive virtual inertia control (J-adaptive $k_J = 5$ and D-fixed $k_D = 0$), in which $D_1 = D_2 = D_3 = 100$, $J_1 = 15, J_2 = 30, J_3 = 45$. The load schedules remain the same as in case 1, and the variations in active power, frequency, RoCoF, J/D parameters are displayed in Fig. 10(a), (b), (c) and (d). When the inverse droop control is employed (RL loads), a significant increase in frequency is observed with the rise in active load. The voltage and current waveforms are presented in Fig. 10(e), while the reactive powers are displayed in Fig. 10(f). From these results, the adjusting time is approximately 2.8s and 2s in the first and second intervals, respectively. The maximum RoCoF occurs around 2.7Hz/s after t=5s. Compared to the J-fixed and D-fixed control, the virtual adaptive inertia control can reduce the adjusting time and initial maximum RoCoF, thereby improving the dynamic frequency performance.

C. CASE 3:SIMULATION WITH J-ADAPTIVE AND D-ADAPTIVE CONDITION

This case is implemented with the proposed method, i.e., J-adaptive ($k_J = 5$) and D-adaptive ($k_D = 0.5$). The simulation parameters of this case are set as follows: $D_1 = D_2 = D_3 = 100$, $J_1 = 15, J_2 = 30, J_3 = 45$. Under the same conditions as Case 1 and Case 2, simulation results of P_i, f_i, RoCoF and J/D variations are exhibited in Fig. 11(a), (b), (c), and (d). The adjusting time reduces to 2s in the first interval and 1.6s in the second interval, with the maximum RoCoF at about 2.3Hz/s. The voltage and current waveforms are depicted in Fig. 11(e), while the reactive powers are presented in Fig. 11(f). Table 4 provides the quantitative comparisons between Case 1, Case 2, and Case 3. It can be observed that oscillations are effectively mitigated with the proposed method. In addition, these simulation results validate the stability performance of the proposed control method.

D. CASE 4:SIMULATION WITH SWITCHING FROM RL TO RC

This simulation is performed under the load switching from RL in [0s, 5s] to RC in [5s, 10s]. The allocations of P_i and Q_i
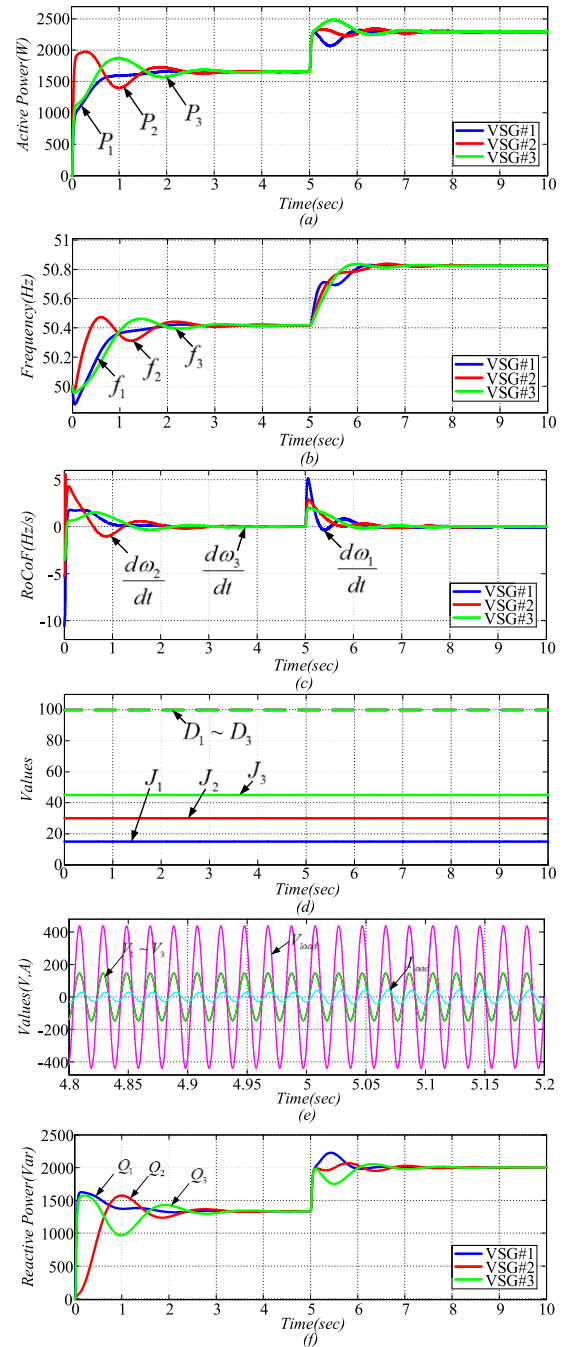

FIGURE 9. Simulation results with the J-fixed and D-fixed condition (a) P_i (b) f_i (c) RoCoF (d) J/D parameters (e) voltage and current waveforms (f) Q_i.

are presented in Fig. 12(a) and (b). The waveforms of f_i are depicted in Fig. 12(c). The voltage and current waveforms are presented in Fig. 12(d). It can be seen that the inverse droop is applied in the first interval, while droop control is used in the second interval. Under the RL or RC loads, the RoCoF curve may exhibit different positive or negative signs. Therefore, the proposed method enables stable operation even when load demands transition from RL loads to RC loads.
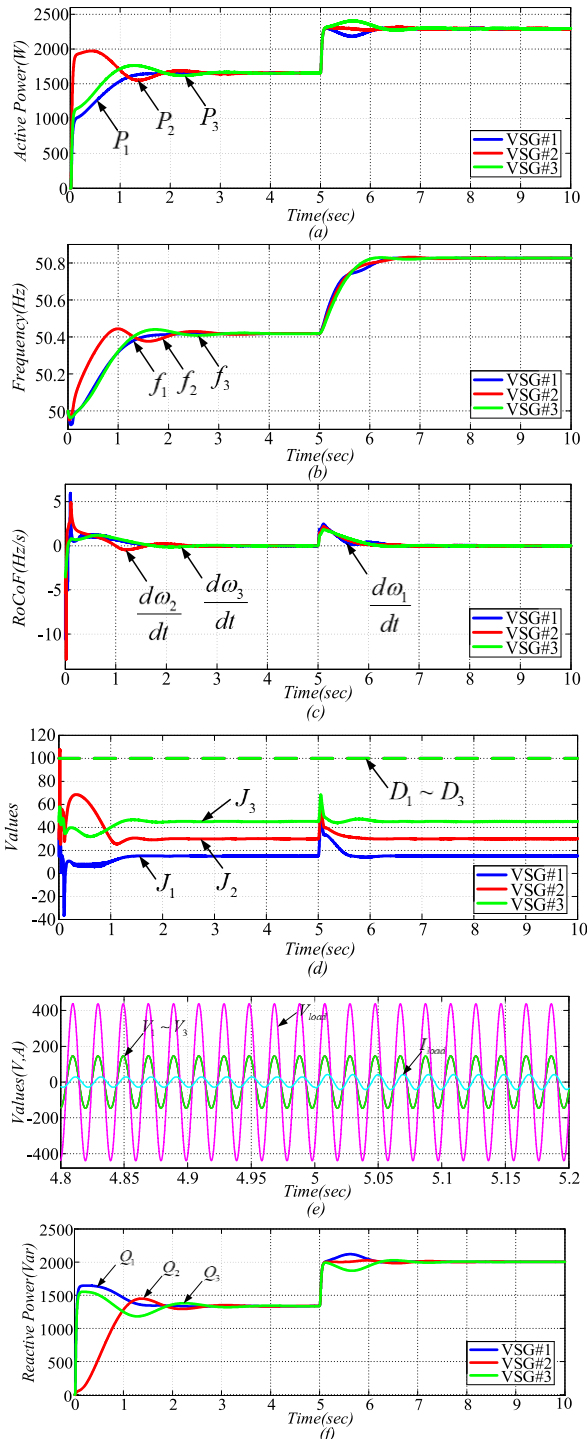
FIGURE 10. Simulation results with the *J*-adaptive and *D*-fixed condition (a) P_i (b) f_i (c) *RoCoF* (d) *J/D* parameters (e) voltage and current waveforms (f) Q_i.
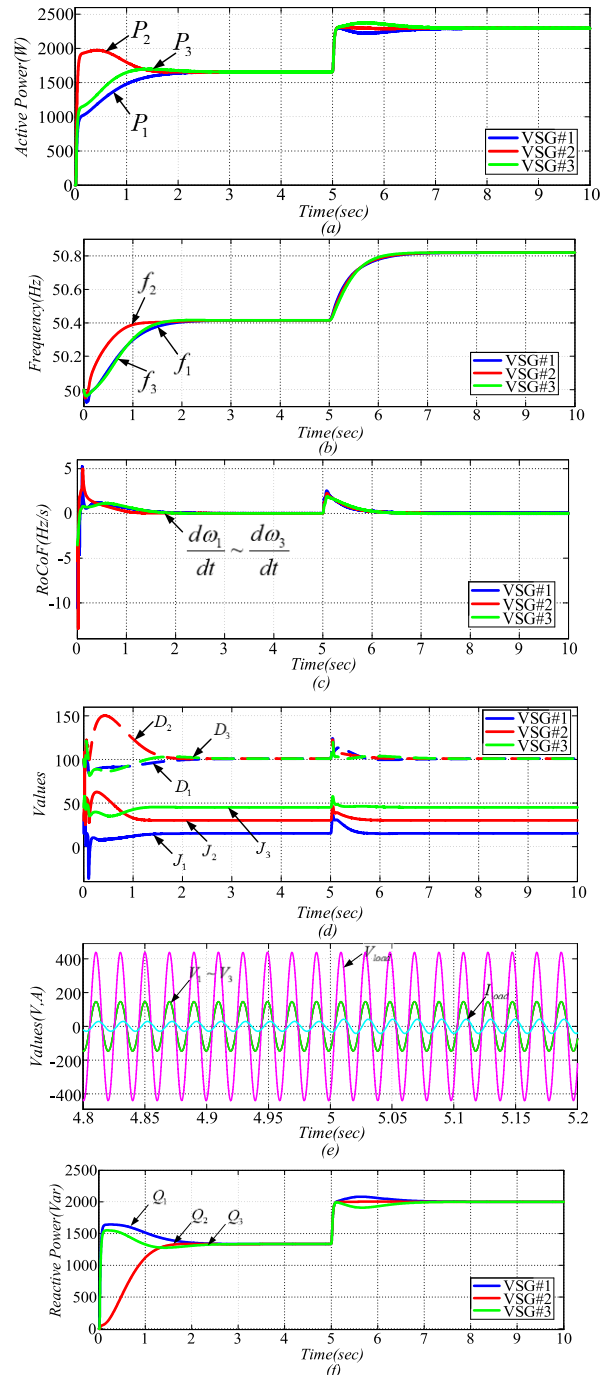

FIGURE 11. Simulation results with the *J*-adaptive and *D*-adaptive condition (a) P_i (b) f_i (c) *RoCoF* (d) *J/D* parameters (e) voltage and current waveforms (f) Q_i.

E. CASE 5: SIMULATION WITH SINGLE-PHASE ASYNCHRONOUS MACHINE

This simulation case is implemented under the asynchronous machine loads condition. At t=5s, a load step is introduced. Initially, the J-fixed and D-fixed control scheme is employed, and the corresponding results of P_i, Q_i and f_i are exhibited in Fig. 13 (a1), (b1), and (c1). Notably, oscillations of frequency

are observed in the depicted plots. Subsequently, the proposed scheme involving adaptive virtual inertia (J-adaptive) and damping (D-adaptive) combination is performed under the same load condition. The results of P_i, Q_i and f_i are displayed in Fig. 13(a2), (b2), and (c2). On comparison, it can be observed that the proposed scheme demonstrates improved frequency regulation in the presence of asynchronous machine load. In addition, the stable operating is guaranteed.
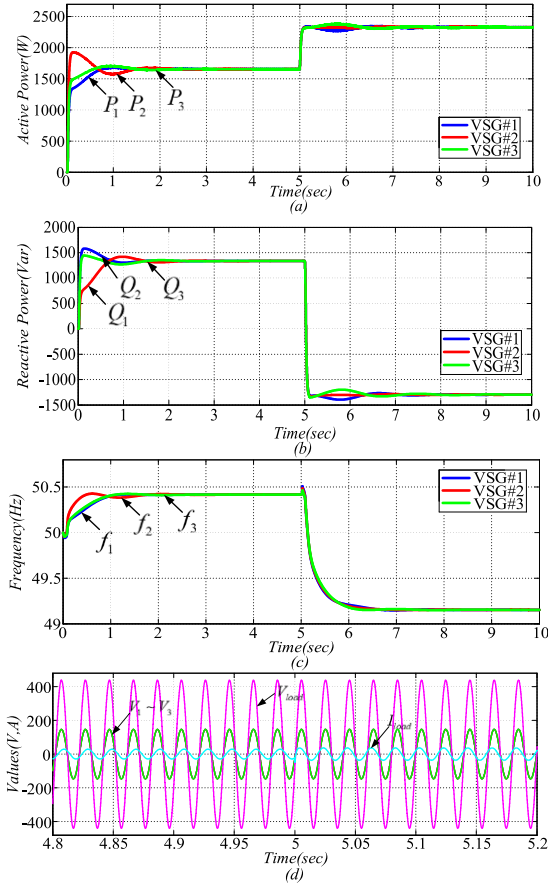
FIGURE 12. Simulation results with load switching (a) P_i (b) Q_i (c) f_i (d) voltage and current waveforms.

TABLE 5. Settings for experiment validations.

Variable	Values	Variable	Values
V^* (V)	110/2	P^* (W)	45
L_{line} (H)	0.5e-3	J_1	1/60
D_1	0.1	J_2	1/120
D_2	0.1	V_{dc1} (V)	66
ω^* (rad/s)	100π	V_{dc2} (V)	66

VI. EXPERIMENT VERIFICATIONS

Limited by the experimental conditions, a cascaded-type VSG experimental prototype involving two VSGs was built in the lab to verify the feasibility of the proposed method, as shown in Fig. 14. Each VSG is controlled by a Rapid Control Prototyping (RCP) YXSPACE controller. The relevant setting parameters can be found in Table 5.

A. CASE 1:PERFORMANCE OF THE J-FIXED AND D-FIXED TERM

In the experimental test, the designed control parameters are configured as: $k_J = 0$, $k_D = 0$. The control methodology involving J-fixed and D-fixed terms is employed. The load step occurs at t=12s. The experimental voltage and current waveforms for the first interval are displayed in Fig. 15. The frequency of VSG#1 and VSG#2 is shown in Fig. 16(a), and
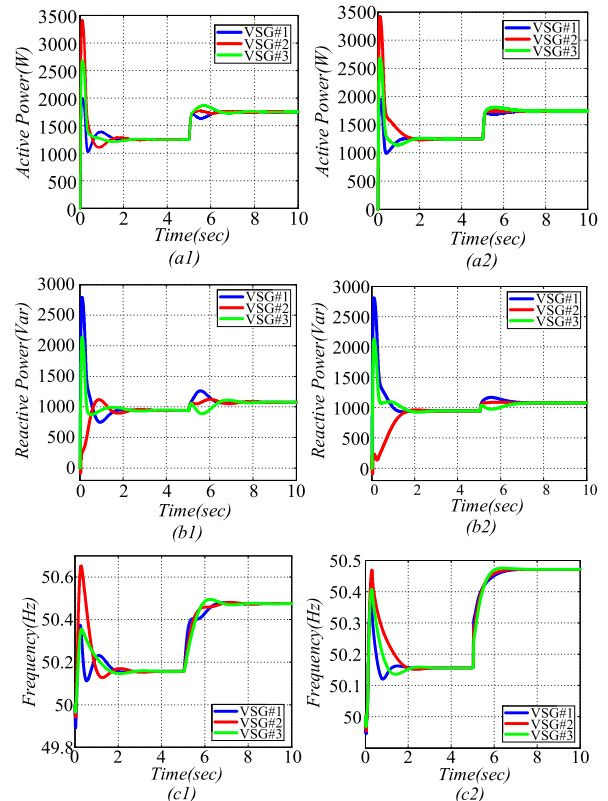

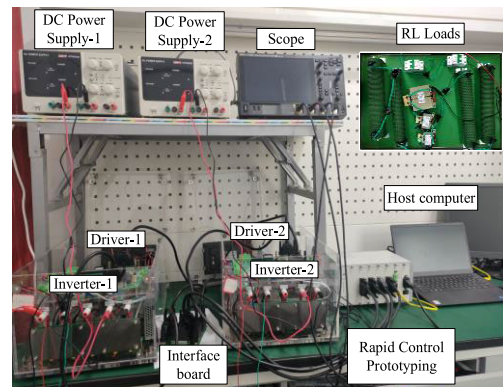FIGURE 13. Comparative results (a) P_i (b) Q_i (c) f_i.

FIGURE 14. Experimental prototype of cascaded-type VSGs.
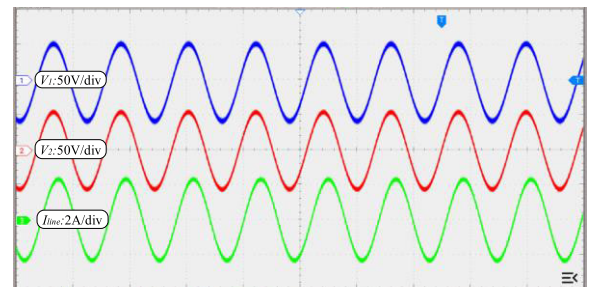

FIGURE 15. Experimental waveform with the J − fixed and D − fixed control.

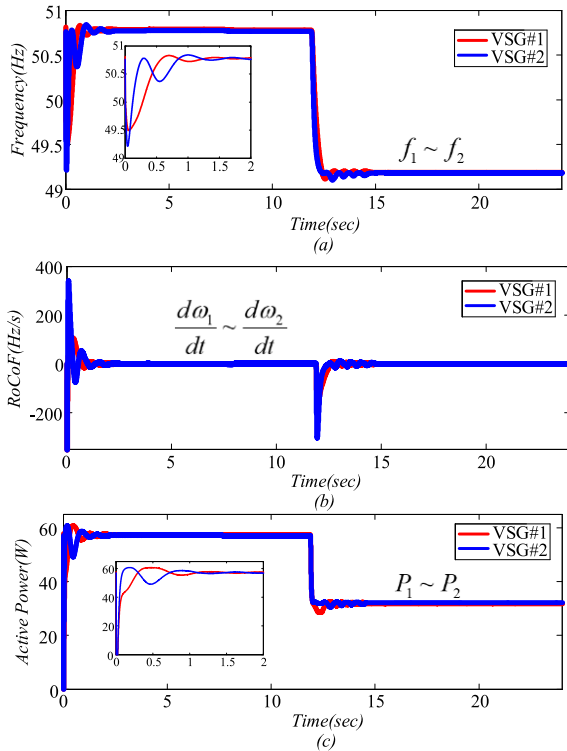the system reaches a steady state after t=1.5s. The results of RoCoF are plotted in Fig. 16(b), with the maximum RoCoF

FIGURE 16. Experimental results with J-fixed and D-fixed control (a) f_i (b) RoCoF (c) P_i.
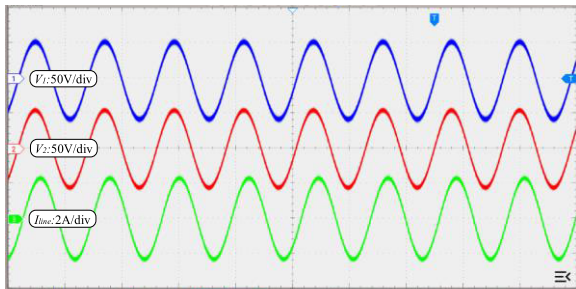

FIGURE 17. Experimental waveform with the $J - fixed$ and $D - fixed$ control.

being approximately 350Hz/s. Further, Fig. 16(c) illustrates the changes in active power over time.

B. CASE 2:PERFORMANCE OF J-ADAPTIVE AND D-ADAPTIVE TERM

The experimental conditions are the same as in case 1. The control scheme employing J-adaptive and D-adaptive terms is carried out, with $k_J = 3e - 4$, $k_D = 0.04$. The load steps at t=9s. The experimental waveforms of voltage and current for the first interval can be seen in Fig. 17. Variations of frequencies over time are displayed in Fig. 18(a), with an adjusting time of approximately 1.1s in the first interval. The *RoCoF* is presented in Fig. 18(b), where the maximum *RoCoF* is about 200Hz/s. Figure 18(c) depicts active power changes over time. Compared with case 1, the proposed method demonstrates the ability to dampen power oscillations and acquire dynamic frequency improvement.
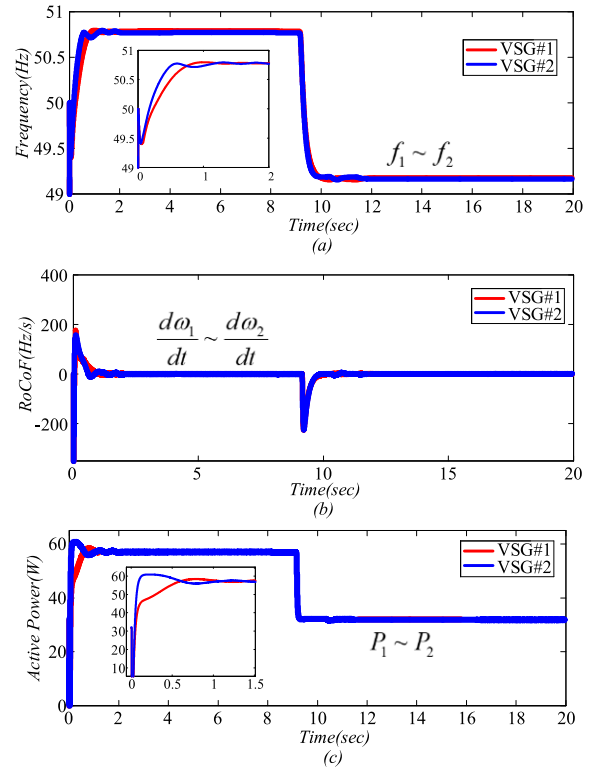

FIGURE 18. Experimental results with J-adaptive and D-adaptive control (a) f_i (b) RoCoF (c) P_i.

VII. CONCLUSION

To solve the problem of oscillations in islanded cascaded-type VSGs, this study proposed a decentralized control that combined adaptive virtual inertia and damping. The dynamic frequency characteristic was revealed for islanded cascaded-type VSGs when inertia and damping parameters changed. An adaptive decentralized control scheme is proposed, incorporating virtual inertia and damping terms to dampen the power and frequency oscillations. Moreover, the design of the main control coefficients is presented. The proposed scheme could effectively suppress the dynamic power and frequency oscillations without impacting the steady-state performance. It can be applied to improve the frequency performance in the dynamic process for islanded cascaded-type VSGs. The results of simulations and experiments have verified the feasibility of the proposed scheme.

Compared to centralized methods, the proposed scheme is a fully communication-free approach. It is especially advantageous in situations where there are a large number of VSGs and significant distances between them. Based on this work, future investigations will consider topics such as the grid-connected mode, the three-phase cascaded-type VSG system, the series-parallel structure, and so on.

REFERENCES

[1] Z. Cao, J. Wang, Q. Zhao, Y. Han, and Y. Li, "Decarbonization scheduling strategy optimization for electricity-gas system considering electric vehicles and refined operation model of power-to-gas," *IEEE Access*, vol. 9, pp. 5716–5733, 2021.

[2] A. H. Alobaidi, S. S. Fazlhashemi, M. Khodayar, J. Wang, and M. E. Khodayar, "Distribution service restoration with renewable energy sources: A review," *IEEE Trans. Sustain. Energy*, vol. 14, no. 2, pp. 1151–1168, Apr. 2023.

[3] X. Li, J. Chai, M. Li, L. Li, and R. You, "A grid frequency support control strategy of the three phase cascaded H-bridge based photovoltaic generation system," *IEEE Access*, vol. 10, pp. 56974–56984, 2022.

[4] S. Bhattacharyya, S. Puchalapalli, and B. Singh, "Operation of grid-connected PV-battery-wind driven DFIG based system," *IEEE Trans. Ind. Appl.*, vol. 58, no. 5, pp. 6448–6458, Sep. 2022.

[5] M. Mao, C. Qian, and Y. Ding, "Decentralized coordination power control for islanding microgrid based on PV/BES-VSG," *CPSS Trans. Power Electron. Appl.*, vol. 3, no. 1, pp. 14–24, Mar. 2018.

[6] Y. Yu and X. Hu, "Active disturbance rejection control strategy for grid-connected photovoltaic inverter based on virtual synchronous generator," *IEEE Access*, vol. 7, pp. 17328–17336, 2019.

[7] L. Xiong, X. Liu, D. Zhang, and Y. Liu, "Rapid power compensation-based frequency response strategy for low-inertia power systems," *IEEE J. Emerg. Sel. Topics Power Electron.*, vol. 9, no. 4, pp. 4500–4513, Aug. 2021.

[8] H. T. Nguyen, G. Yang, A. H. Nielsen, and P. H. Jensen, "Combination of synchronous condenser and synthetic inertia for frequency stability enhancement in low-inertia systems," *IEEE Trans. Sustain. Energy*, vol. 10, no. 3, pp. 997–1005, Jul. 2019.

[9] A. Fathi, Q. Shafiee, and H. Bevrani, "Robust frequency control of microgrids using an extended virtual synchronous generator," *IEEE Trans. Power Syst.*, vol. 33, no. 6, pp. 6289–6297, Nov. 2018.

[10] K. Jiang, H. Su, H. Lin, K. He, H. Zeng, and Y. Che, "A practical secondary frequency control strategy for virtual synchronous generator," *IEEE Trans. Smart Grid*, vol. 11, no. 3, pp. 2734–2736, May 2020.

[11] S. Chen, Y. Sun, H. Han, G. Shi, Y. Guan, and J. M. Guerrero, "Dynamic frequency performance analysis and improvement for parallel VSG systems considering virtual inertia and damping coefficient," *IEEE J. Emerg. Sel. Topics Power Electron.*, vol. 11, no. 1, pp. 478–489, Feb. 2023.

[12] H. Cheng, W. Huang, C. Shen, Y. Peng, Z. Shuai, and Z. J. Shen, "Transient voltage stability of paralleled synchronous and virtual synchronous generators with induction motor loads," *IEEE Trans. Smart Grid*, vol. 12, no. 6, pp. 4983–4999, Nov. 2021.

[13] Z. Shuai, W. Huang, Z. J. Shen, A. Luo, and Z. Tian, "Active power oscillation and suppression techniques between two parallel synchronverters during load fluctuations," *IEEE Trans. Power Electron.*, vol. 35, no. 4, pp. 4127–4142, Apr. 2020.

[14] S. Zhang, J. Kang, and J. Yuan, "Analysis and suppression of oscillation in V/F controlled induction motor drive systems," *IEEE Trans. Transport. Electrific.*, vol. 8, no. 2, pp. 1566–1574, Jun. 2022.

[15] K. Shi, W. Song, H. Ge, P. Xu, Y. Yang, and F. Blaabjerg, "Transient analysis of microgrids with parallel synchronous generators and virtual synchronous generators," *IEEE Trans. Energy Convers.*, vol. 35, no. 1, pp. 95–105, Mar. 2020.

[16] Y. Yu, S. K. Chaudhary, G. D. A. Tinajero, L. Xu, N. N. B. A. Bakar, J. C. Vasquez, and J. M. Guerrero, "A reference-feedforward-based damping method for virtual synchronous generator control," *IEEE Trans. Power Electron.*, vol. 37, no. 7, pp. 7566–7571, Jul. 2022.

[17] M. Chen, D. Zhou, and F. Blaabjerg, "Active power oscillation damping based on acceleration control in paralleled virtual synchronous generators system," *IEEE Trans. Power Electron.*, vol. 36, no. 8, pp. 9501–9510, Aug. 2021.

[18] X. Hou, Y. Sun, X. Zhang, J. Lu, P. Wang, and J. M. Guerrero, "Improvement of frequency regulation in VSG-based AC microgrid via adaptive virtual inertia," *IEEE Trans. Power Electron.*, vol. 35, no. 2, pp. 1589–1602, Feb. 2020.

[19] P. Liu, Y. Bi, and C. Liu, "Data-based intelligent frequency control of VSG via adaptive virtual inertia emulation," *IEEE Syst. J.*, vol. 16, no. 3, pp. 3917–3926, Sep. 2022.

[20] J. Alipoor, Y. Miura, and T. Ise, "Power system stabilization using virtual synchronous generator with alternating moment of inertia," *IEEE J. Emerg. Sel. Topics Power Electron.*, vol. 3, no. 2, pp. 451–458, Jun. 2015.

[21] A. Karimi, Y. Khayat, M. Naderi, T. Dragicevic, R. Mirzaei, F. Blaabjerg, and H. Bevrani, "Inertia response improvement in AC microgrids: A fuzzy-based virtual synchronous generator control," *IEEE Trans. Power Electron.*, vol. 35, no. 4, pp. 4321–4331, Apr. 2020.

[22] A. S. Mir and N. Senroy, "Self-tuning neural predictive control scheme for ultrabattery to emulate a virtual synchronous machine in autonomous power systems," *IEEE Trans. Neural Netw. Learn. Syst.*, vol. 31, no. 1, pp. 136–147, Jan. 2020.

[23] D. Li, Q. Zhu, S. Lin, and X. Y. Bian, "A self-adaptive inertia and damping combination control of VSG to support frequency stability," *IEEE Trans. Energy Convers.*, vol. 32, no. 1, pp. 397–398, Mar. 2017.

[24] L. Huang, H. Xin, H. Yuan, G. Wang, and P. Ju, "Damping effect of virtual synchronous machines provided by a dynamical virtual impedance," *IEEE Trans. Energy Convers.*, vol. 36, no. 1, pp. 570–573, Mar. 2021.

[25] S. Das, I. U. Nutkani, and C. A. Teixeira, "Decentralized master–slave control for series-cascaded islanded AC microgrid," *IEEE Trans. Ind. Electron.*, vol. 69, no. 6, pp. 5942–5951, Jun. 2022.

[26] M. Lu, S. Dutta, and B. Johnson, "Self-synchronizing cascaded inverters with virtual oscillator control," *IEEE Trans. Power Electron.*, vol. 37, no. 6, pp. 6424–6436, Jun. 2022.

[27] J. He, Y. Li, B. Liang, and C. Wang, "Inverse power factor droop control for decentralized power sharing in series-connected-microconverters-based islanding microgrids," *IEEE Trans. Ind. Electron.*, vol. 64, no. 9, pp. 7444–7454, Sep. 2017.

[28] L. Li, Y. Sun, H. Han, X. Hou, M. Su, and Z. Liu, "Power factor angle consistency control for decentralised power sharing in cascaded-type microgrid," *IET Generat., Transmiss. Distrib.*, vol. 13, no. 6, pp. 850–857, Mar. 2019.

[29] L. Li, Y. Sun, Z. Liu, X. Hou, G. Shi, and M. Su, "A decentralized control with unique equilibrium point for cascaded-type microgrid," *IEEE Trans. Sustain. Energy*, vol. 10, no. 1, pp. 324–326, Jan. 2019.

[30] L. Li, Y. Sun, and S. Fu, "Decentralized mutual damping control of cascaded-type VSGs for power and frequency oscillation suppression," *IEEE Trans. Ind. Electron.*, vol. 69, no. 10, pp. 10215–10226, Oct. 2022.

[31] L. Li, Y. Sun, Y. Liu, P. Tian, and S. Shen, "A communication-free adaptive virtual inertia control of cascaded-type VSGs for power oscillation suppression," *Int. J. Electr. Power Energy Syst.*, vol. 149, Jul. 2023, Art. no. 109034.

[32] S. Fu, Y. Sun, L. Li, Z. Liu, H. Han, and M. Su, "Power oscillation suppression of multi-VSG grid via decentralized mutual damping control," *IEEE Trans. Ind. Electron.*, vol. 69, no. 10, pp. 10202–10214, Oct. 2022.

LANG LI was born in Guizhou, China, in 1992. He received the B.S. degree in electrical engineering and automation from Guizhou University, Guiyang, China, in 2015, and the M.S. degree in electrical engineering and the Ph.D. degree in control science and engineering from Central South University, Changsha, China, in 2018 and 2021, respectively. He is currently an Associate Professor with the Department of Automation, Moutai Institute. His research interests include distributed microgrids and power-electronic-enabled power networks.

KE ZHOU was born in Henan, China, in 1977. He received the B.S. and M.S. degrees from the Guizhou University of Technology, China, and the Ph.D. degree from the Nanjing University of Posts and Telecommunications, China. He was a Research Fellow with Guizhou Power Grid Company Ltd. He was an Associate Professor with Guizhou University. He is currently a Professor with the Department of Automation, Moutai Institute. His research interests include microgrids and smart grids.

PENG TIAN was born in Sichuan, China, in 1991. He received the B.S. and Ph.D. degrees in automation and power electronic equipment and systems from Guizhou University, Guiyang, China, in 2014 and 2021, respectively. He is currently an Associate Professor with the Department of Automation, Moutai Institute. His research interests include control of wind turbine, stability analysis of the power systems, and smart grids.

· · ·